

## Article

# High-Frequency Lacustrine Lithological and Geochemical Variations in the Eocene Qaidam Basin: Implications for Paleoenvironment Reconstruction

Kunyu Wu <sup>1,2,3</sup>, Xiucheng Tan <sup>2,4,5,\*</sup>, Xiangjun Liu <sup>2,\*</sup>, Peng Pang <sup>2,4,5</sup>, Songtao Wu <sup>3</sup>, Shituan Xue <sup>6</sup>, Haoting Xing <sup>3,7</sup>, Ying Xiong <sup>8</sup>, Yafeng Li <sup>3</sup>, Menglin Zhang <sup>3</sup>, Wei Deng <sup>2,4,5</sup> and Juan Wang <sup>3</sup>

<sup>1</sup> Petroleum Engineering School, Southwest Petroleum University, Chengdu 610500, China; wukunyu1986@126.com

<sup>2</sup> State Key Laboratory of Oil and Gas Reservoir Geology and Exploitation, Southwest Petroleum University, Chengdu 610500, China

<sup>3</sup> Research Institute of Exploration and Development of Qinghai Oil Field Company, CNPC, Dunhuang 736202, China

<sup>4</sup> SWPU Division of Key Laboratory of Carbonate Reservoirs, CNPC, Chengdu 610500, China

<sup>5</sup> Natural Gas Geology Key Laboratory of Sichuan Province, Southwest Petroleum University, Chengdu 610500, China

<sup>6</sup> Oilfield Development Department of Qinghai Oil Field Company, PetroChina Qinghai Oil Field Company, Dunhuang 736202, China

<sup>7</sup> Plateau Saline Lake Basin Oil and Gas Geology Key Laboratory of Qinghai Province, PetroChina Qinghai Oil Field Company, Dunhuang 736202, China

<sup>8</sup> School of Earth and Space Sciences, Peking University, Beijing 100871, China

\* Correspondence: tanxiucheng70@163.com (X.T.); liuxiangjunswpi@163.com (X.L.)

**Abstract:** Lacustrine sedimentary processes exhibit high sensitivity to paleoenvironmental changes, often manifesting as high-frequency sedimentary cycles that control the complex variations in sedimentary structure, mineral composition, and element distribution. However, the intricate co-variation mechanism among paleoclimate and paleowater properties at a high precision level (centimeter to meter scale) is still controversial. This study focuses on conducting a high-frequency cycle analysis of lacustrine mixed rocks from the Eocene Lower Ganchaigou Formation (LGCG) in the Qaidam Basin, employing petrology, mineralogy, organic geochemistry, and elemental geochemistry techniques. The lithological variation was characterized by the superposition of three lithofacies types from the bottom to the top with a single sequence: massive sandstone, laminated silty shale, and bedded calcareous dolostone. Geochemical data revealed cyclical variations in the paleoenvironment in the vertical profile, which conformed to the high-frequency lithofacies cycles. Based on the reconstruction of the lake level and paleowater properties, a synthesized paleoclimate–sedimentary model that comprised three consecutive periods within an individual sequence was established. From the bottom to the top of each cycle, the Eocene paleoenvironment varied from reduction and desalination to oxidation and salinization, which was controlled by a decline in the lake level resulting from a transformation of the paleoclimate from warm and humid to cold and arid. The variations in petrology and geochemistry observed in the Eocene Qaidam Basin play a crucial role in comprehending the sedimentary response to paleoenvironmental changes at high precision levels within lacustrine settings.

**Keywords:** lacustrine mixed rock; high-frequency cycles; organic–inorganic geochemistry; paleoenvironment; paleoclimate



**Citation:** Wu, K.; Tan, X.; Liu, X.; Pang, P.; Wu, S.; Xue, S.; Xing, H.; Xiong, Y.; Li, Y.; Zhang, M.; et al. High-Frequency Lacustrine Lithological and Geochemical Variations in the Eocene Qaidam Basin: Implications for Paleoenvironment Reconstruction. *Minerals* **2024**, *14*, 79. <https://doi.org/10.3390/min14010079>

Academic Editor: Aleksey Sadekov

Received: 17 November 2023

Revised: 5 January 2024

Accepted: 8 January 2024

Published: 10 January 2024



**Copyright:** © 2024 by the authors. Licensee MDPI, Basel, Switzerland. This article is an open access article distributed under the terms and conditions of the Creative Commons Attribution (CC BY) license (<https://creativecommons.org/licenses/by/4.0/>).

## 1. Introduction

The integration of Earth science and astronomy research has revealed the cyclic variations in Earth's climate controlled by changes in Earth's orbital parameters [1–3]. These cyclical variations in paleoclimate signals can be recorded in sedimentary systems that are

sensitive to paleoenvironment changes [4,5]. The sedimentary cycle refers to a sequence of sediments formed by sedimentation and deposition conditions in the same order, resulting in periodic changes in the structure, lithology, and lithofacies of sediments. High-frequency sedimentary cycles are high-frequency cyclical responses to sea-level fluctuations and climate oscillations driven by periodic changes in Earth's orbital forcing [5,6]. Additionally, high-frequency sedimentary cycles play a significant control role in organic matter enrichment and the distribution of carbonate pore spaces [7]. Therefore, the analysis of high-frequency sedimentary cycles is not only beneficial for uncovering essential scientific questions related to paleoclimatic evolution and paleoenvironmental reconstruction, but also can provide valuable guidance for oil and gas exploration practices. In particular, the co-variation mechanism of paleoclimate and paleowater properties in saline lake basins at a high precision level remains to be explored.

Mixed sedimentary systems are widely developed in various sedimentary environments, including marine environments [8–10], freshwater lakes [11], and saline lakes [12]. The formation of mixed rocks is typically the result of the interaction and coupling of numerous factors, such as clastic material supply, paleoclimate, water body conditions, and water level fluctuations [13,14]. Moreover, mixed sedimentation holds significant implications in petroleum exploration. In particular, fine-grained mixed sedimentation often exhibits favorable source–reservoir relationships, such as proximity to source rocks or coeval source–reservoir systems, providing a foundation for hydrocarbon accumulation within mixed sediments [15]. Therefore, comprehensive research on mixed sedimentation is of great significance for paleoenvironment reconstruction and related oil and gas exploration. Previous studies on mixed depositional systems have primarily focused on marine environments [8,10,16], with relatively fewer investigations into lacustrine settings. Moreover, the traditional genesis types of mixed sedimentation, proposed for shallow marine shelf environments, fail to accurately explain the mechanisms of complex mixed sedimentation in continental basins, as they only consider the manner in which sediments are mixed [15]. In recent years, the significance of lacustrine mixed rocks has been increasingly highlighted, as they have been identified as high-quality reservoirs for hydrocarbon accumulation [17]. Currently, high-frequency sedimentary cycle analyses are predominantly applied to clastic rocks and carbonate rocks, with relatively limited focus on mixed rocks [18,19]. The formation of mixed rocks is controlled by multiple factors, resulting in greater research challenges compared to clastic or carbonate rocks, especially concerning the reconstruction of sedimentary environments. Therefore, the distinctiveness of high-frequency cycle analysis may hold the key to addressing scientific questions regarding lacustrine mixed rocks.

The Qaidam Basin, located in the northeastern part of the Tibet Plateau, is a Cenozoic saline basin in China (Figure 1a). Its thick and high-frequency variational mixed sediments of the Neogene serve as crucial archives for studying the paleoclimate, paleoenvironment, and tectonic uplift of the Tibet Plateau since the collision between the Indian and Eurasian plates [12]. Additionally, the Yingxiongling area of the Qaidam Basin exhibits globally distinctive giant saline lacustrine shale oil reservoirs within the Paleogene Lower Ganchaigou Formation (LGCG), indicating promising prospects for oil and gas exploration [17]. Currently, due to the significant discoveries and favorable exploration prospects of unconventional oil and gas in the LGCG, numerous scholars have focused on the characterization, identification, and evaluation of the mixed rock reservoirs in this area [20–23]. However, studies related to the subdivision of sequences in fine-grained sediments, and the paleoclimatic significance of this extensive and thick mixed rock succession, are still lacking and remain controversial. For instance, ref. [24] employed evaporites as a primary marker layer to identify the initial lake flood surface area and subdivide the high-frequency sequence of the evaporite-bearing series in the LGCG. However, this subdivision scheme has regional limitations, and may not be applicable in areas where evaporites are absent. The authors of [25] suggested that the LGCG was located in a dry, cold, and anoxic reducing environment. Furthermore, ref. [12] demonstrated that the initial uplift of the Altyn Mountains

in the Eocene and global cooling led to a reduction in moisture transport to the Qaidam Basin. The authors of [26] also observed that the uplift of the Tibetan Plateau resulted in a significant burial of organic and inorganic carbon due to the accumulation of substantial amounts of silicates in the lake. The highly crystalline silicate debris streams from the Altyn Tagh Mountains accumulated in the lake, releasing N, S, K, Na, and trace elements, which provided materials for the carbonate-rich and eutrophic lake. However, rare reports have been found in these studies regarding the analysis of paleoenvironment and paleoclimate variations within the high-frequency cycles.

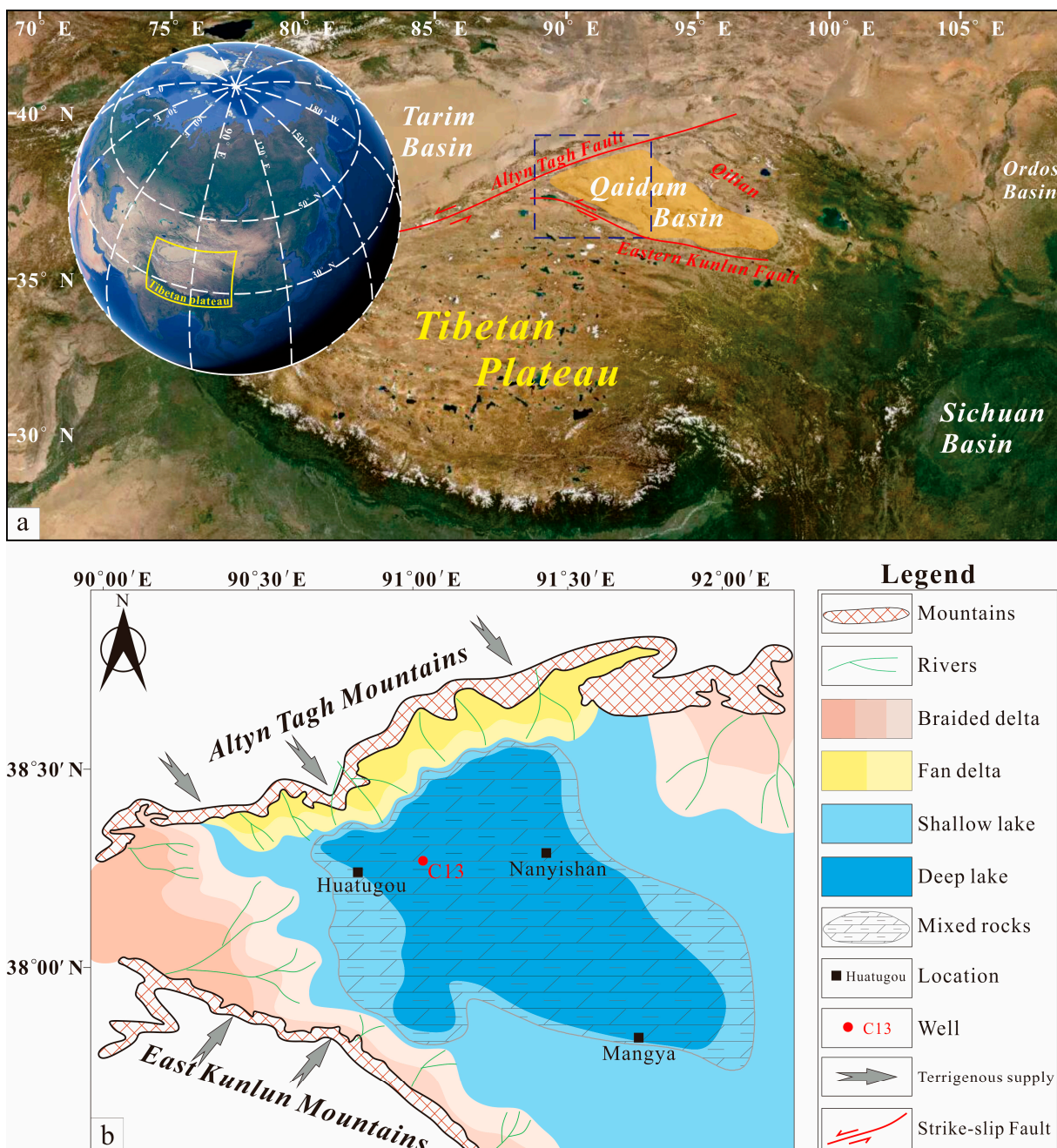


**Figure 1.** (a) Satellite images of the Tibet Plateau. The yellow box indicates the extent of the Tibetan Plateau, and the light yellow shading indicates the location of the Qaidam Basin. The blue rectangle marks the location of (b); (b) paleogeographic map and distribution of mixed rocks of the southwestern Qaidam Basin during deposition of the LGCG in the Eocene.

In this study, a combination of petrological, mineralogical, and geochemical analysis for the lacustrine mixed rocks of the LGCG was conducted to reconstruct the sedimentary processes and paleoenvironment of the Qaidam Basin. Our research offers a new perspective for understanding the high-frequency paleoenvironmental changes and climatic fluctuations resulting from the uplift of the Tibet Plateau in the Eocene.

## 2. Geological Settings

The Qaidam Basin is situated in the northern Tibet Plateau, surrounded by the East Kunlun Mountains, Qilian Mountains, and Altyn Tagh Mountains, with an average elevation of 2950 m (Figure 1a). It covers an area of  $9.6 \times 10^4$  km<sup>2</sup>, and was a large lacustrine intermountain basin in western China with hydrocarbon-bearing formations in the Cenozoic [17,27]. Since the Cenozoic, under the tectonic movement of the Himalayas and the intense uplift of the Tibet Plateau, the basin's current structural features have gradually been formed through the joint control of the sinistral strike-slip faults of the Eastern Kunlun and the Altyn Fault [28,29] (Figure 1a). The continuous uplift of the Tibet Plateau had significant effects on the paleo-sedimentary environment, paleo-tectonic pattern, and basin evolution. The paleo-altitudes around the basin have been continuously rising, resulting in basin closure and a progressively drier and colder climate [30]. Against this backdrop, during the sedimentary period of the LGCG in the western Qaidam basin, the paleoclimate was relatively arid, with intense evaporation, and the water body became weakly saline for an extended period. Additionally, due to simultaneous terrestrial input from the peripheral delta sedimentary system, the mineral composition in the western Qaidam Basin is complex and diverse, displaying typical characteristics of mixed sedimentation [31]. Influenced by the difference in tectonic compression during different periods, this area exhibited distinct paleotopographical characteristics with alternating uplifted and subsided regions. Therefore, in the whole sedimentary environment of semi-deep to shallow lake subfacies, microfacies types such as gypsum pans, sandy shoals, saline lakes, and muddy dolomitic semi-deep lakes can be observed [32] (Figure 1b).

The Cenozoic strata in this area can be divided into six formations from bottom to top: Lulehe Formation ( $E_{1+2}$ ), LGCG ( $E_3$ ), Upper Ganchaigou Formation ( $N_1$ ), Lower Youshashan Formation ( $N_2^1$ ), Upper Youshashan Formation ( $N_2^2$ ), and Shizigou Formation ( $N_3^2$ ) (Figure 2). The upper section of LGCG ( $E_3^2$ ) represents the maximum flooding period with the deepest water level and the finest sediment grain size, making it the primary target for unconventional oil and gas exploration in the western Qaidam Basin [33]. The lithological and mineralogical composition of this unit is complex, consisting of terrigenous clastics, clay minerals, carbonate minerals, and evaporite minerals [34,35]. Notably, terrigenous clastic-carbonate mixed rocks are the predominant lithology in the LGCG. Additionally, the sedimentary responses affected by fluctuations in the lake level in the LGCG are sensitive and significant. The composition and structure of the rock change frequently and are well preserved, reflecting a cyclical high-frequency vertical superimposed lake level fluctuation sedimentary cycle; thus, the rock is an important material reflecting the sedimentary environment and paleoclimatic evolution.

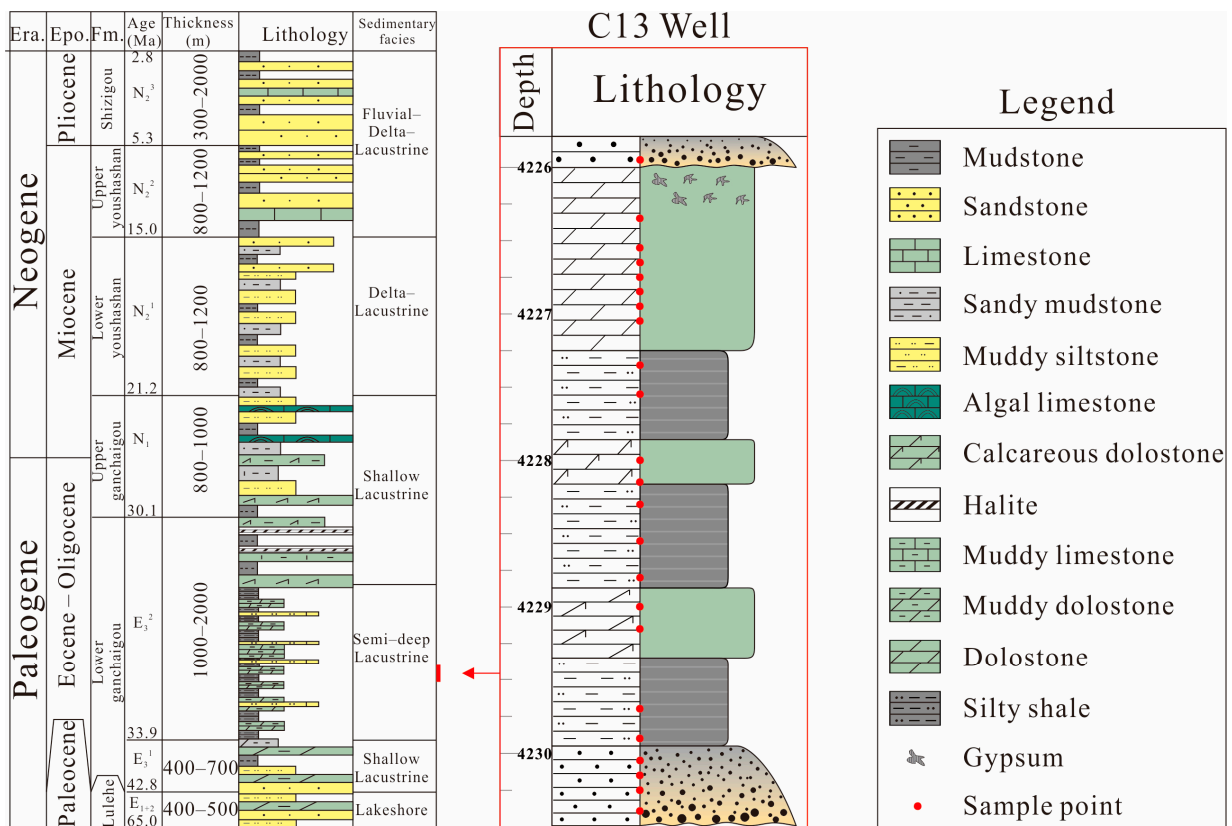


**Figure 2.** Schematic stratigraphic column of the Yingxiongling area (based on [17]) and sedimentary profile of Well C13. Lithofacies in the lithology channel of Well C13 refer to the legend shown on the right side of the figure.

### 3. Materials and Methods

The lithofacies of C13 changes frequently and the coring is complete, characterized by high-frequency cyclic deposition in the whole Eocene LGCG, which is suitable for high-frequency cycle analysis. To characterize the paleoenvironmental changes in high-frequency cycles, 23 samples were collected continuously at a depth interval of 4225–4231 m from the LGCG of Well C13 in the western part of the Qaidam Basin for element geochemical and isotope analysis. This 6 m core is representative of a set of cycles from a much larger cyclical interval (Figure 2). To determine mineralogical variations within the cycles, 22 samples were consecutively collected from the same depth interval for whole-rock X-ray diffraction (XRD) testing. Corresponding core photos and micrographs were obtained from the digital core library, Exploration and Development Institute of PetroChina Qinghai Oil Field Company, Dunhuang, China, to identify the high-frequency sedimentary cycles.

#### 3.1. Mineralogical Measurements

The whole-rock XRD test was conducted using an Empyrean Ruiying diffractometer with monochromatic Cu and  $K\alpha$  radiation. Pretreatment and analytical procedures were performed on all samples at the Laboratory Center, Exploration and Development Institute of PetroChina Qinghai Oil Field Company, Dunhuang, China.

#### 3.2. Carbon and Oxygen Isotopes

The inorganic carbon and oxygen isotopes in the 23 samples were tested using a multi-purpose online gas preparation instrument (GasBench-II, Thermo Fisher Scientific Inc., Bremen, Germany) linked to a stable isotope mass spectrometer (MAT 253Plus, Thermo Fisher Scientific Inc., Bremen, Germany) at the SWPU Division of Key Laboratory of

Carbonate Reservoirs, China National Petroleum Corporation, Chengdu, China. Firstly, a fixed mass of powder sample (100 mg) was added to the reaction flask and sealed, and the flask was vacuumized with high-purity He gas to eliminate the effect of air in the flask on the determination of isotope ratios. The carbonate was then reacted with phosphoric acid at 70 °C, and the released gases were passed through a gas chromatographic column to separate CO<sub>2</sub> from other impurity gases. Finally, the separated CO<sub>2</sub> was carried by He gas to a stable isotope mass spectrometer for isotope ratio detection. The  $\delta^{13}\text{C}_{\text{CaCO}_3}$  and  $\delta^{18}\text{O}_{\text{CaCO}_3}$  ratios were analyzed using the international standard Vienna Pee Dee Belemnite as the reference standard with a laboratory precision of  $\pm 0.2\%$ .

### 3.3. Element Geochemical Analysis

Considering the complexity of the mineral composition of mixed rocks in the Gan-chaiyou area, major and trace element analysis was performed on three different fractions of the bulk samples, acetic leachate, acetic residue, and whole rock, to evaluate the elemental chemical properties of carbonate minerals and clastic minerals, respectively. The 23 samples were separated evenly into two groups. One group of the whole rock was melted at 1050 °C for 15 min for whole-rock major element analysis. The flux was lithium tetraborate–lithium metaborate–lithium fluoride (45:10:5), the oxidant was ammonium nitrate, and the release agent was lithium bromide. The loss on ignition (LOI) was obtained by measuring the weight loss after melting the sample. The prepared glass pellets were subjected to whole-rock major element analysis using a wavelength-dispersive X-ray fluorescence spectrometer (ZSXPrimus II) produced by Rigaku Corporation, Japan. The K $\alpha$  lines were employed for the analysis of major elements, and the standard curve was constructed using the national standard reference material series, with a relative standard deviation (RSD) of <2%. For trace element analysis of acetic leachate and acetic residue, another group of the whole rock was dissolved in mol L<sup>-1</sup> at 60 °C for 24 h. Then, the supernatant leachate and residue were collected separately by centrifugation and drying. For final analysis, the prepared leachate and residue were reacted, respectively, with a mixture of high-purity nitric acid and hydrofluoric acid at 190 °C for 24 h. The prepared reaction solution was used for trace element analysis using an ELEMENT ICP-MS (Agilent 7700e, Agilent Technology Co., Ltd., Santa Clara, CA, USA) at the Wuhan SampleSolution Analysis Technology Co., Ltd., Wuhan, China.

## 4. Results

### 4.1. Lithology

Three primary lithofacies have been identified based on the rock structure and mineral composition.

#### 4.1.1. Massive Sandstones

In the core, massive sandstone exhibits a light gray color with a massive (>1 m) and positive grain sequence structure, and erosional surfaces are commonly observed at the base of the lithofacies (Figure 3A,J). Under the microscope, it displays a sandy texture, mainly composed of feldspar, quartz, and rock debris, with moderate sorting and rounding, and the pore space is infilled with calcite and mud (Figure 3a,i). At the top of this lithofacies, there is a transition to laminated silty shale, while at the bottom, there is an abrupt change into bedded calcareous dolostone.

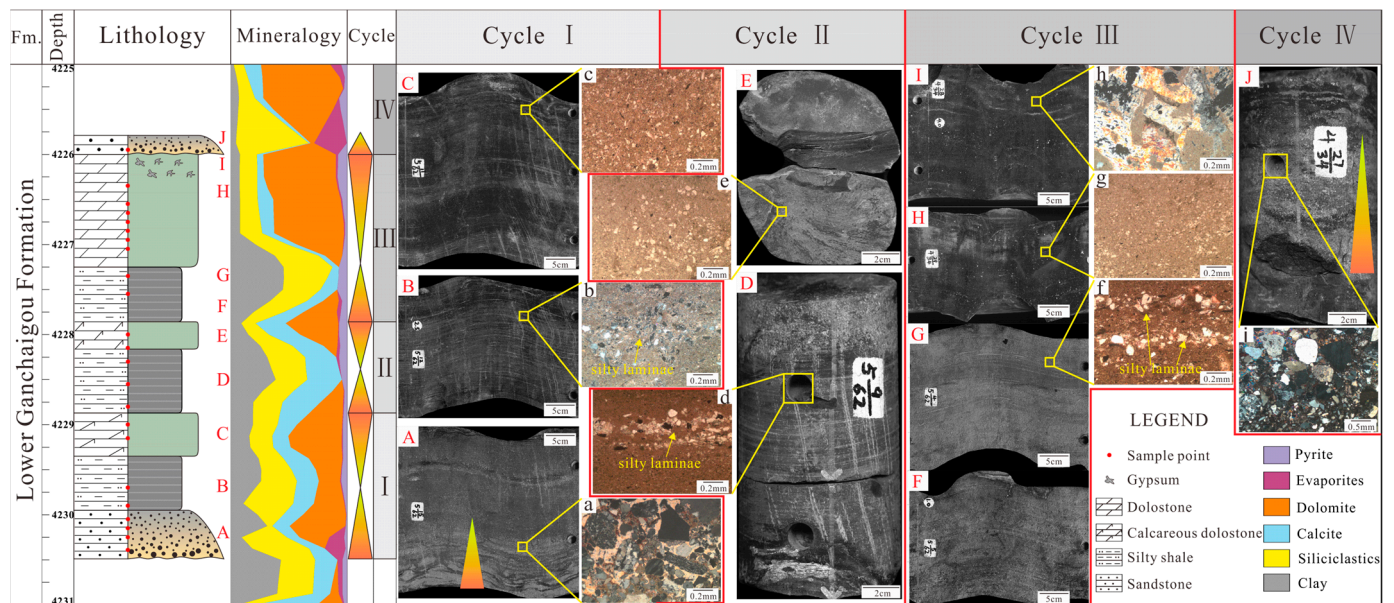


**Figure 3.** Lithologic characteristics of the high-frequency cycles in Well C13. (A) core, positive grain sequence structure, 4230.25 m; (B) core, 4229.77 m; (C) core, 4229 m; (D) core, 4228.5 m; (E) core, 4228.1 m; (F) core, 4227.74 m; (G) core, 4227.4 m; (H) core, 4226.45 m; (I) core, 4226.18 m; (J) core, positive grain sequence structure, 4225.95 m; (a) thin section within (A), massive sandstone; (b) thin section within (B), laminated silty shale; (c) thin section within (C), bedded calcareous dolostone; (d) thin section within (D), laminated silty shale; (e) thin section within (E), bedded calcareous dolostone; (f) thin section within (G), laminated silty shale; (g) thin section within (H), bedded calcareous dolostone; (h) thin section within (I), bedded calcareous dolostone with glauberite-anhydrite aggregates; (i) thin section within (J), massive sandstone.

#### 4.1.2. Laminated Silty Shales

In the core, laminated silty shale exhibits a dark gray color and a laminated structure (<1 cm, Figure 3B,D,F,G). Under the microscope, this lithofacies is mainly composed of clay minerals, silt-sized siliciclastic fragments, and a minor amount of micritic carbonate minerals, and the silt-sized siliceous debris is mostly horizontally distributed (Figure 3b,d,f). The top of the lithofacies abruptly changes into bedded calcareous dolostones, and the bottom is connected with massive clastic rocks or bedded calcareous dolostones.

#### 4.1.3. Bedded Calcareous Dolostones

In the core, bedded calcareous dolostone exhibits a gray color and bedded structure (several centimeters to tens of centimeters, Figure 3C,E,H,I). Under the microscope, it mainly consists of carbonate minerals with a micritic texture and minor amounts of silt-sized siliciclastic fragments (Figure 3c,e,g). At the top of this lithofacies, there is a sharp transition to clastic rocks, while at the bottom, it transitions to laminated silty shale. Glauberite-anhydrite aggregates are frequently observed at the top of this lithofacies, appearing as white clusters in the core (Figure 3H,I) and exhibiting coarse crystal structures and individual forms under the microscope, ranging from 2 mm to 1 cm in size (Figure 3h).

#### 4.1.4. High-Frequency Sedimentary Cycle Division

Based on periodic and frequent changes in the sediment stacking pattern and mineral composition, the profile of Well C13 was divided into three high-frequency cycles (Cycles I–III) with a thickness of 1–2 m (Figure 3). Above the interface of individual cycles, the initial sedimentation of a new cycle predominates, characterized by relatively quiet and low-energy sedimentary conditions. This includes laminated silty shale or terrigenous debris deposits brought in by the initial flooding of the lake, which has distinct lithofacies

mutations with the bedded gypsum-bearing calcareous dolostone below the interface. Below the interface of individual cycles, there are predominantly bedded gypsum-bearing calcareous dolostones, reflecting the shallowing of the lake water and increased salinity during the late stage of a single sedimentary cycle.

#### 4.2. Mineralogy

A mineral composition ternary plot is shown in Figure 4, indicating a complex mixture of sediments composed of carbonate, clay, and siliceous clasts. Further information can be found in the Supplementary Materials under Table S1. The vertical distribution of mineral composition along the well section is illustrated in Figure 3, suggesting a clear periodic and frequent superposition of mineral compositional variations with the high-frequency sedimentary cycles. In the lower part of a single high-frequency sedimentary cycle, the main minerals are clay (avg. 27.0%) and quartz (avg. 21.3%), followed by calcite (avg. 18.4%) and dolomite/Fe-dolomite (avg. 13.1%), with lesser amounts of plagioclase (avg. 8.7%), pyrite (avg. 3.4%), gypsum (avg. 3.2%), and K-feldspar (avg. 1.3%). In the upper part of high-frequency sedimentary cycles, the dominant minerals are dolomite/Fe-dolomite (avg. 47.2%), followed by calcite (avg. 14.2%), clay (avg. 13.5%), and quartz (avg. 11.8%), with minor amounts of plagioclase (avg. 6.3%), pyrite (avg. 4.5%), gypsum (avg. 1.3%), and K-feldspar (avg. 0.4%).

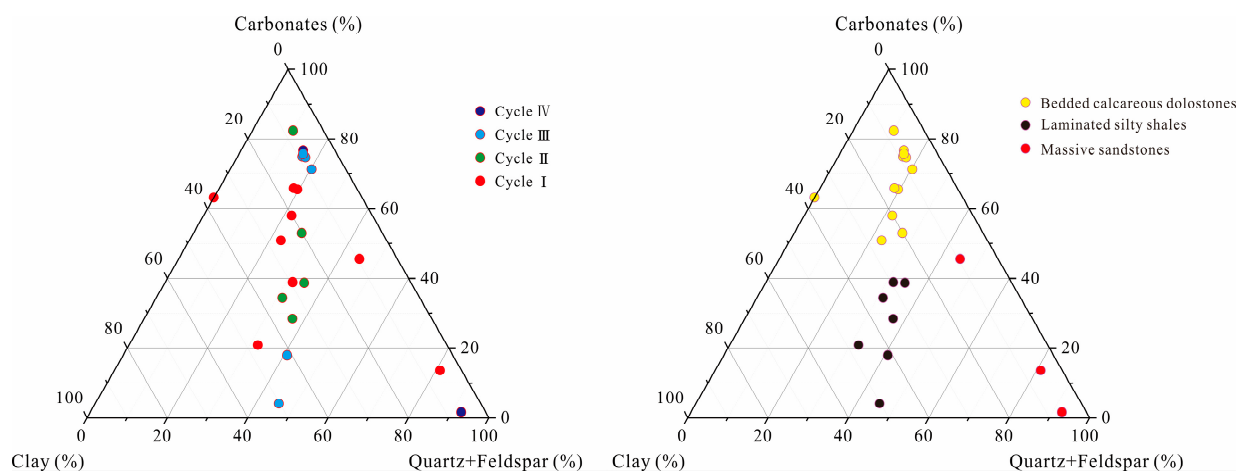


**Figure 4.** Ternary diagram of the mineralogical compositions of the studied bulk samples.

#### 4.3. C and O Isotopes Analysis

Overall, 23 samples from Well C13 yield  $\delta^{13}\text{C}$  values ranging from  $-1.70\text{‰}$  to  $-0.69\text{‰}$  (avg.  $-1.20\text{‰}$ , VPDB) and  $\delta^{18}\text{O}$  values ranging from  $-7.97\text{‰}$  to  $-1.78\text{‰}$  (avg.  $-4.89\text{‰}$ , VPDB). Further information can be found in the Supplementary Materials under Table S2. The vertical distribution of each parameter is shown in Figure 5. It is evident that these parameters exhibit cyclic and frequent superposition variations with the high-frequency sedimentary cycles. In the upper part of the high-frequency sedimentary cycles, TOC (avg. 0.25%) shows relatively low values, while porosity (avg. 5.48%),  $\delta^{13}\text{C}$  (avg.  $-1.01\text{‰}$ , VPDB), and  $\delta^{18}\text{O}$  (avg.  $-3.06\text{‰}$ , VPDB) exhibit relatively high values. In the lower part of the high-frequency sedimentary cycles, TOC (avg. 0.37%) shows relatively high values, whereas porosity (avg. 0.71%),  $\delta^{13}\text{C}$  (avg.  $-1.42\text{‰}$ , VPDB), and  $\delta^{18}\text{O}$  (avg.  $-6.82\text{‰}$ , VPDB) display relatively low values.

#### 4.4. Element Geochemistry

The measured concentrations of major, trace, and rare-earth elements in the samples are listed in Table S3. Among them, the measured values of major elements and trace and rare-earth elements are derived from bulk samples and acetic leachate, respectively.

Meanwhile, the enrichment index calculations using the mean of post-Archean Australian Shale (PAAS; data from [36]) are plotted in Figure 6.

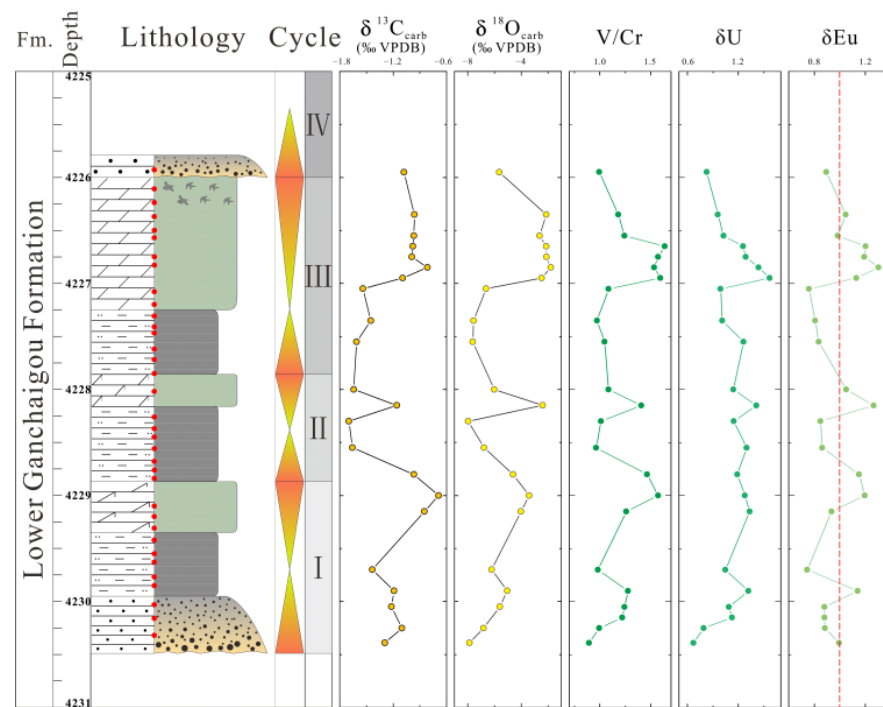


**Figure 5.** Stratigraphic distribution of the C and O isotopes, trace elements in high-frequency cycles.

Among the major elements, the contents of MgO and CaO are much higher than in the post-Archean Australian Shale (PAAS), and the contents of Na<sub>2</sub>O are slightly higher than in the PAAS, whereas the contents of the remaining major elements are relatively lower than those in the PAAS (Figure 6a). Relatively high contents of MgO and CaO are probably related to the high contents of carbonate minerals in the mixed rocks of LGCG, especially in the upper part of the high-frequency cycles (Figure 3).

Overall, there are significant differences in the concentrations of trace elements in the acetic leachate, ranging from 0.001 µg/g to 1000 µg/g (Figure 6b), which indicates that the leachate was separated relatively cleanly and the debris were rarely mixed. Among them, only the Sr content (avg. 946 µg/g) is notably higher than that of PAAS, which is possibly related to the depositional environment of the saline lake basin in the LGCG. Additionally, the concentrations of Zr, Nb, and Cs are particularly low, with average values of 0.036, 0.004, and 0.018 µg/g, respectively.

The total amount of rare-earth elements ( $\Sigma\text{REE}$ ) in the LGCG samples was determined to range from 13.1 to 52.5 µg/g, with an average of 35.7 µg/g (Figure 6), which is lower than the PAAS (184.77 µg/g; data from [36]). The mean value of light rare-earth elements (LREEs: La–Eu) is 31.5 µg/g, which is higher than the heavy rare-earth element (HREEs: Gd–Lu) content (avg. 4.2 µg/g). The high  $\Sigma\text{LREE}/\Sigma\text{HREE}$  values (avg. 7.4) also show an obvious differentiation between the LREE and HREE. In addition, it was found that the PAAS-normalized REE patterns of all samples are similar, showing upper sloping LREE and lower sloping HREE trends (Figure 6c).

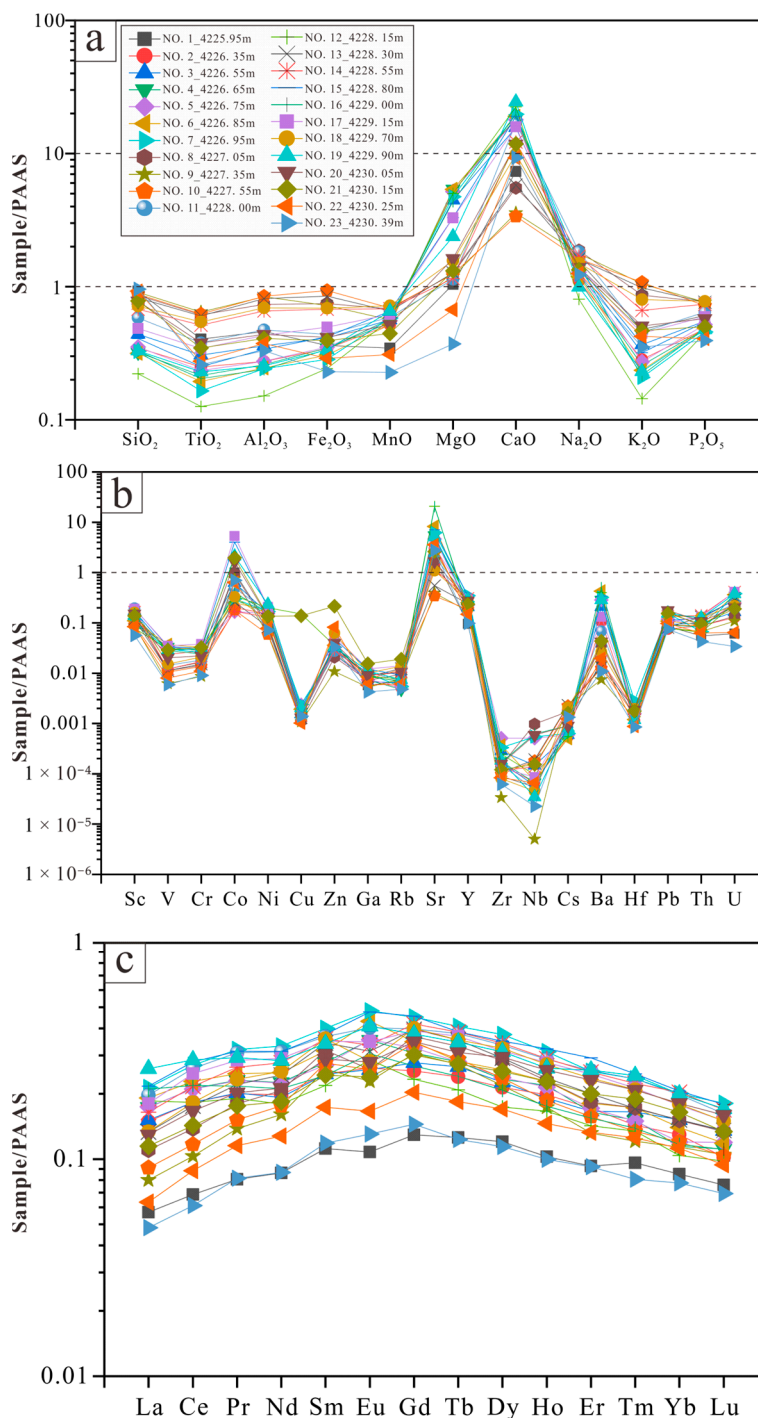


**Figure 6.** Concentration coefficient of the samples versus post-Archean Australian Shale (PAAS): (a) major elements; (b) trace elements; (c) rare-earth elements.

**5. Discussion**

*5.1. Water Hydrochemistry in Paleolake Basin*

*5.1.1. Paleosalinity*

During the Eocene, the Qaidam Basin was a saline lacustrine environment in an intermontane basin [12,37,38]. Using petrographic observation and mineralogical analysis, three superimposed high-frequency sedimentary cycles were identified in the sampling section from the LGCG (Figure 3). Generally, a complete sequence consists of massive argillaceous sandstones in the lower part, followed by laminated silty shales, and then is

dominated by thin- to thick-bedded calcareous dolostones in the upper part. The presence of glauberite–anhydrite aggregation in the bedded calcareous dolostones indicates an increase in water salinity within the high-frequency cycle.

The isotopic signals of carbonate precipitated from original water are widely used as reliable proxies for analyzing water salinity and environmental changes [39]. During the process of evaporation, based on the isotope fractionation effect, the vapor phase becomes enriched in light isotopes, while the liquid concentrate becomes enriched in heavy isotopes. In modern open freshwater lakes, the  $\delta^{13}\text{C}$  and  $\delta^{18}\text{O}$  of primary carbonates are negative and fall into the third quadrant in the cross-plot of  $\delta^{13}\text{C}$  and  $\delta^{18}\text{O}$ , whereas the  $\delta^{13}\text{C}$  of closed saline lakes is largely positive and falls into the first or second quadrant [40–42]. In these three high-frequency cycles, the  $\delta^{13}\text{C}$  and  $\delta^{18}\text{O}$  values of all carbonate components are negative, and fall collectively in the transition zone between closed saline lakes and open freshwater lakes (Figure 7). Inside the cycles, the carbon and oxygen isotope values of the bedded calcareous dolostones in the upper part of the cycles are significantly higher than those of the massive sandstone and laminated silty shales in the lower part of the cycles (Figure 7a). Moreover, the carbon and oxygen isotope values of the massive sandstone and laminated silty shale mostly fall within the range of open freshwater lakes, while the carbon and oxygen isotope values of the bedded calcareous dolostones predominantly fall within the range of closed saline lakes (Figure 7b). This observation suggests a gradual restriction and salinization of the water body within individual sedimentary cycles. This conclusion was also supported by previous studies. By comparing the carbon and oxygen isotopic compositions of the western Qaidam Basin with typical modern lacustrine carbonate sediments, refs. [12,43] concluded that the western Qaidam Basin is a semi-closed lacustrine environment. However, their studies lack a discussion of changes in the water environment inside the high-frequency cycles.

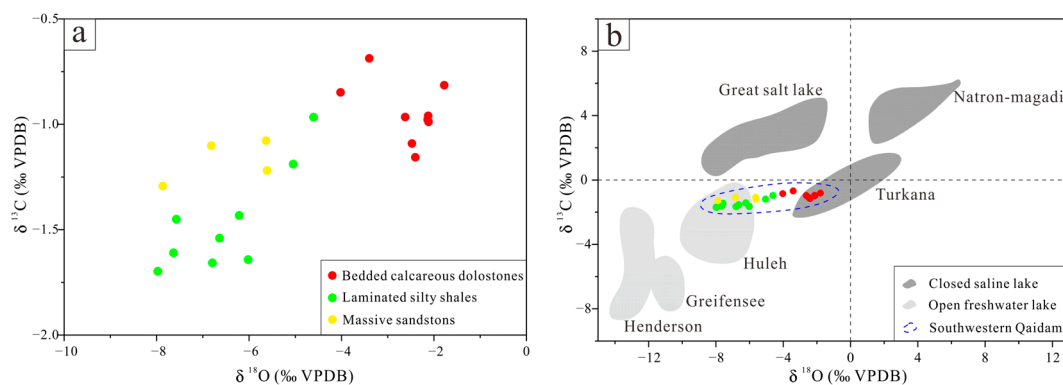


**Figure 7.** Cross-plot of  $\delta^{13}\text{C}$  and  $\delta^{18}\text{O}$  values of the carbonate components of the samples from the LGCG formation: (a) cross-plot from three lithofacies in high-frequency cycle; (b) a comparison of the southwestern Qaidam with typical modern lakes (the range of modern lakes is based on [12], with data originating from [40,44]).

### 5.1.2. Redox Conditions

Trace elements have been widely employed in reconstructing redox environments [45–47]. Some redox-sensitive elements will exhibit different geochemical behaviors, such as precipitation or dissolution, in different redox environments [48–50]. Therefore, the concentrations and ratios of these elements could be used as effective proxies for paleoredox environment reconstruction [51,52]. The use of these paleoredox indicators was suggested based on the premise that these elements are authigenic without exogenous input effects [53,54]. The elemental composition of carbonate components in mixed deposits is more suitable for paleoredox analysis than that of bulk samples [12]. In this study, the redox-sensitive elements (U, V, and Cr) of the bulk phase show a highly positive relationship ( $R^2 > 0.77$ ) with immobile elements (Al and Ti) derived from detrital sources (Figure 8). On the contrary, there is no significant correlation between Al and these redox-sensitive

elements of the leachate treated with acetic acid ( $R^2 < 0.47$ , Figure 8b–d). Therefore, the measured element concentrations of acetic leachate in this study have removed the influence of exogenous debris input and can be used for paleoenvironmental reconstruction. Generally, U and V are dissolved with a high valence state in lake water under oxidizing conditions, while they are precipitated with a low valence state in deposits under reducing conditions [53,55]. Hence, a higher U/Th or V/Cr ratio from the leachate phase indicates a shallower and more oxic lake water environment. In our study, the V/Cr ratios and  $\delta U$  ( $\delta U = 2U/(U + Th/3)$ ) in the upper of three high-frequency cycles are all significantly higher than those in the lower part (Figure 5), which indicates the relatively low lake level and oxic conditions in the upper part of high-frequency cycles.

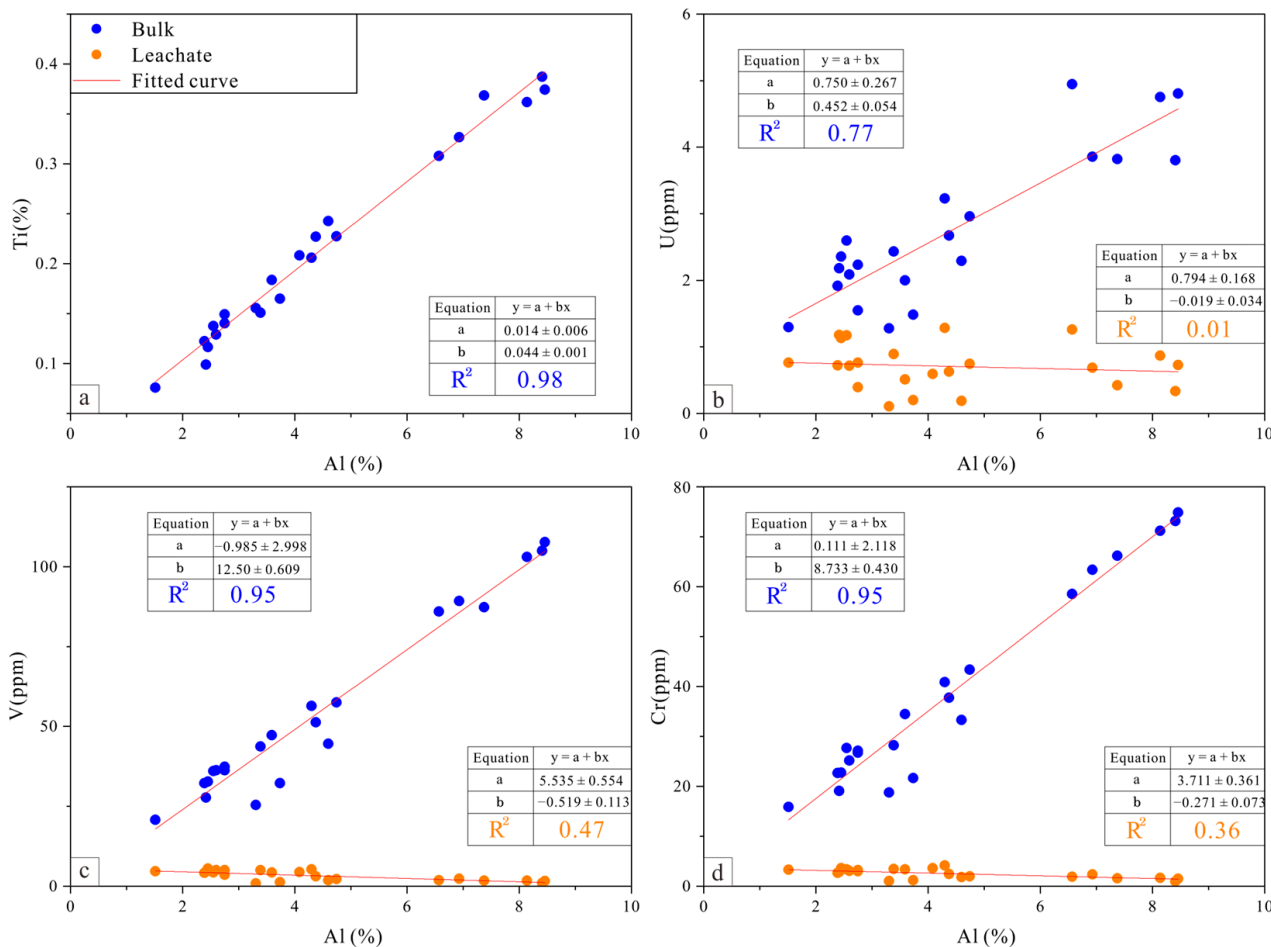


**Figure 8.** Scatter plots of (a) Al and Ti; (b) Al and U; (c) Al and V; (d) Al and Cr. The blue and orange spheres indicate the elemental composition of the bulk samples and the acetic leachate, respectively.

In rare-earth elements, Ce and Eu anomalies can also be used to identify the redox environment; they are also dissolved in lake water under oxic conditions and enriched in deposits under reducing conditions [56,57]. In this study, the  $\delta Ce$  and  $\delta Eu$  values show evident positive anomalies in the upper part of the high-frequency cycles, with an average of 1.04 and 1.14, respectively. In contrast, they present negative anomalies at the bottom and average 0.98 and 0.80, respectively (Figure 5). These rare-earth element indicators also prove the process of the gradual decline in and oxidation of lake water within high-frequency cycles.

### 5.2. Paleoclimate Reconstruction

#### 5.2.1. Constraints from Element Geochemistry

The depletion or enrichment of trace elements in water and deposits is not only related to the physical and chemical conditions of sedimentary media, but is also controlled by paleoclimate conditions [58]. Therefore, the content and ratio of trace elements in deposits can provide reliable information on paleoclimatic changes [45,51]. Cu and Al are generally transported to basins through organic matter and terrigenous debris, so they are highly sensitive to the paleoclimate and weathering conditions of the source area [12,46]. Conventionally, the wetness of the climate is inversely proportional to the Na/Al and Sr/Cu ratios [46,59], but is proportional to the Rb/Sr ratio [60,61]. The Al<sub>2</sub>O<sub>3</sub>/MgO ratio of major elements in deposits can also reflect the changes in the paleoclimate. Under arid climates, a large amount of Mg is precipitated from the lake water, which is attributed to the alkaline enhancement of the lake water caused by strong evaporation. Hence, a higher Al<sub>2</sub>O<sub>3</sub>/MgO ratio reflects warm and humid climates, and a lower ratio indicates arid climates [62,63]. The mixed deposits of the LGCG exhibit a trend of Sr/Cu and Na/Al ratios gradually decreasing and then increasing within a single high-frequency cycle, while the Rb/Sr and Al<sub>2</sub>O<sub>3</sub>/MgO ratios show the opposite (Figure 9). This suggests a strong coupling between climate changes and the high-frequency cyclic sedimentation of mixed rocks. Within a single high-frequency cycle, the paleoclimate became warm and humid with the transgression in the early stage, and then gradually became arid with the decrease in water level in the later stage. The period of laminated silty shale deposition corresponds to the most humid and warm climate conditions.

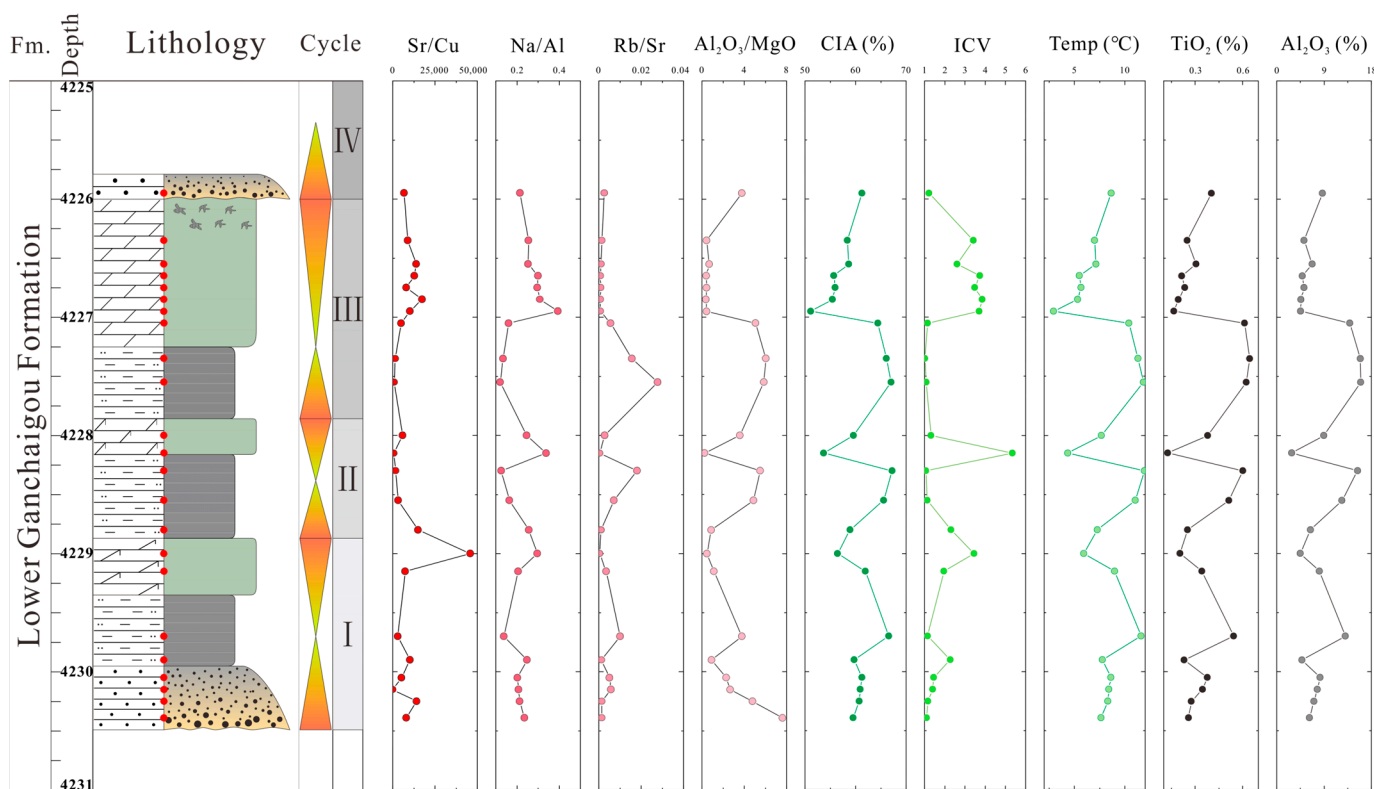


**Figure 9.** Vertical variations in proxies of paleoclimate, weathering degree, and debris input in the LGCG.

#### 5.2.2. Chemical Weathering Intensity

Studies have suggested that changes in paleoclimate often result in a series of disturbances in terrestrial ecosystems around the basin. For example, warm and humid climates can intensify the chemical weathering of rocks and soils, leading to alterations

in the living environment of terrestrial organisms [59,64,65]. As the loss of alkaline substances during weathering process is relatively easy to measure, parameters related to major elements are commonly used by scholars to quantitatively analyze the weathering intensity and paleoclimate of the source area, including chemical index of alteration (CIA), chemical index of weathering (CIW), and plagioclase index of alteration (PIA) [59,66–68]. Among them, CIA, calculated using Equation (1), has been widely used to investigate the intensity of weathering caused by paleoclimatic changes and ‘deep-time’ major climatic events [69–71]. The CIA value is directly proportional to the weathering intensity caused by paleoclimatic change. The authors in [67] proposed that CIA values within the range of 50 to 60, 60 to 80, and 80 to 100, correspond to weak weathering, moderate weathering, and strong weathering, respectively.

$$CIA = Al_2O_3 / (Al_2O_3 + K_2O + Na_2O + CaO^*) \times 100, \quad (1)$$

$$CaO^* = \min(CaO - 10/3 \times P_2O_5, Na_2O) \quad (2)$$

$$ICV = (Fe_2O_3 + K_2O + Na_2O + CaO + MgO + MnO + TiO_2) / Al_2O_3 \quad (3)$$

$$Temp = 0.56 \times CIA - 25.7 \quad (4)$$

To exclude the influence of CaO contained in carbonate and phosphate minerals that are not closely related to weathering, only CaO in the silicate minerals was selected as CaO\* in our study, following the approach of [66]. Subsequently, Equation (2), proposed by [72], was utilized to calculate the CIA values. In addition, the effects of sedimentary differentiation and recycling also need to be considered when using CIA values to determine the weathering intensity in a source area. In this study, the index of compositional variability (ICV), calculated using Equation (3), was employed to exclude the effect of recycling on the CIA value. Samples with an ICV value greater than 1 represent immature argillaceous rocks containing high amounts of non-clay silicate minerals, which are the initial deposits under tectonic activity and can eliminate the influence of recycling [73,74]. All of the mixed rock samples from the LGCG in this study showed ICV values greater than 1 (Figure 9), indicating that none of the samples had undergone a recycling process. As shown in Figure 9, the CIA values of the lower part of the three high-frequency cycles are distributed between 60% and 70%, with an average of 63.5%, indicating a moderate degree of weathering. However, the CIA values of the upper part of the cycles range from 50% to 60% and average 56.8%, which suggests weak weathering [67].

Considering that potassium metasomatism during diagenesis can lead to an underestimation of CIA values, the  $Al_2O_3$ –(CaO\* + Na<sub>2</sub>O)–K<sub>2</sub>O (A–CN–K) ternary diagram and CIA<sub>corr</sub> values were introduced to correct the CIA value of the samples that experienced potassium metasomatism, following the approach of [66,75] (Figure 10). In this study, no significant difference was observed between the corrected CIA<sub>corr</sub> value and the original CIA value. The results also show that the laminated silty shales and massive sandstones at the bottom of the cycles have relatively high CIA<sub>corr</sub> values, indicating warm and humid paleoclimates. In contrast, the bedded calcareous dolostones in the upper part of the cycles have relatively low CIA<sub>corr</sub> values, reflecting cold and arid paleoclimates (Figure 10). This phenomenon implies a decrease in paleotemperature and an increase in drought intensity within a single high-frequency cycle, which is consistent with the paleoclimate change characteristics indicated by the trace element ratio.

In order to quantify the relationship between paleoclimates and chemical weathering intensity, Equation (4) was proposed by [68] to calculate the temperature of land surface (Temp, °C) based on CIA values, and has been extensively used in paleoclimate reconstructions [76–79]. The changes in surface temperature during the high-frequency cycles of the LGCG are illustrated in Figure 9. The average surface temperature in the early stage of the high-frequency cycles is 11.2 °C, which is significantly higher than the average temperature of 6.1 °C in the later stage.

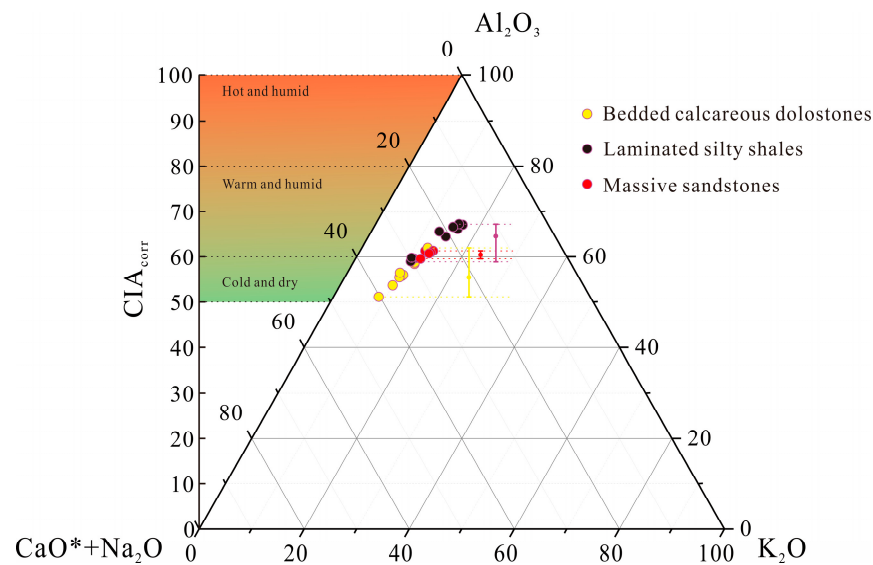


**Figure 10.** Ternary phase diagram of A-CN-K and  $CIA_{corr}$  changes in the samples of the LGCG.

### 5.2.3. Terrigenous Clastic Input

As the oxides of Al and Ti are mostly present in detrital minerals (clay and heavy minerals) of terrigenous origin, the contents of  $Al_2O_3$  and  $TiO_2$  have been widely used to characterize the input of terrigenous debris [59,80]. In this study, the  $Al_2O_3$  and  $TiO_2$  contents in the early stage of the high-frequency cycles are significantly higher than those in the later stage, with average values of 12.2% and 0.6%, respectively (Figure 9). This observation indicates a greater input of terrigenous debris during the lake transgression process, encompassing both clay minerals and heavy minerals. Coupled with the changes in paleoclimate and water properties discussed earlier, the elevated terrigenous debris input during the lake transgression period aligns well with the intensification of weathering and the increase in surface runoff resulting from the warm and humid paleoclimate. This conclusion is consistent with findings from other continental basins, such as the Lucaoguo Formation in the Junggar Basin [81] and the Santanghu Basin [80].

### 5.3. Synthesized Paleoclimate–Sedimentary Model

The western Qaidam Basin was a plateau saline lake in the Eocene, and it featured a series of high-frequency superimposed mixed sedimentary sequences with a cumulative thickness exceeding 1200 m [17,82]. In the study of mixed sediments from the Yingxi area of the Qaidam Basin, ref. [83] demonstrated that the high-frequency deposition sequences were largely influenced by lake level changes resulting from paleoclimate variations. The lithological and geochemical evidence presented in this study further confirms the high-frequency periodic variations in water properties and paleoclimate during the Eocene in the Qaidam Basin. Hence, building upon the variations in the lake level and corresponding paleowater properties in the Eocene western Qaidam Basin, and considering previous research on lacustrine mixed rocks in the Qaidam Basin [12,26,83], we established a synthesized paleoclimate–sedimentary model in lacustrine mixed rocks for three consecutive periods within a whole high-frequency cycle (Figure 11).

During the initial flooding period, the lake basin was in a semi-open state, and the paleoclimate was temperate and semi-humid, accompanied by moderate weathering and land runoff (detrital input). Under these paleoclimatic conditions, rainfall slightly exceeded evaporation, causing the lake level to rise, resulting in a dysoxic–suboxic and desalinated water condition. At the bottom of the lake, numerous laminated limestone-bearing silty shales and some massive sandstones were deposited (Figure 11a).

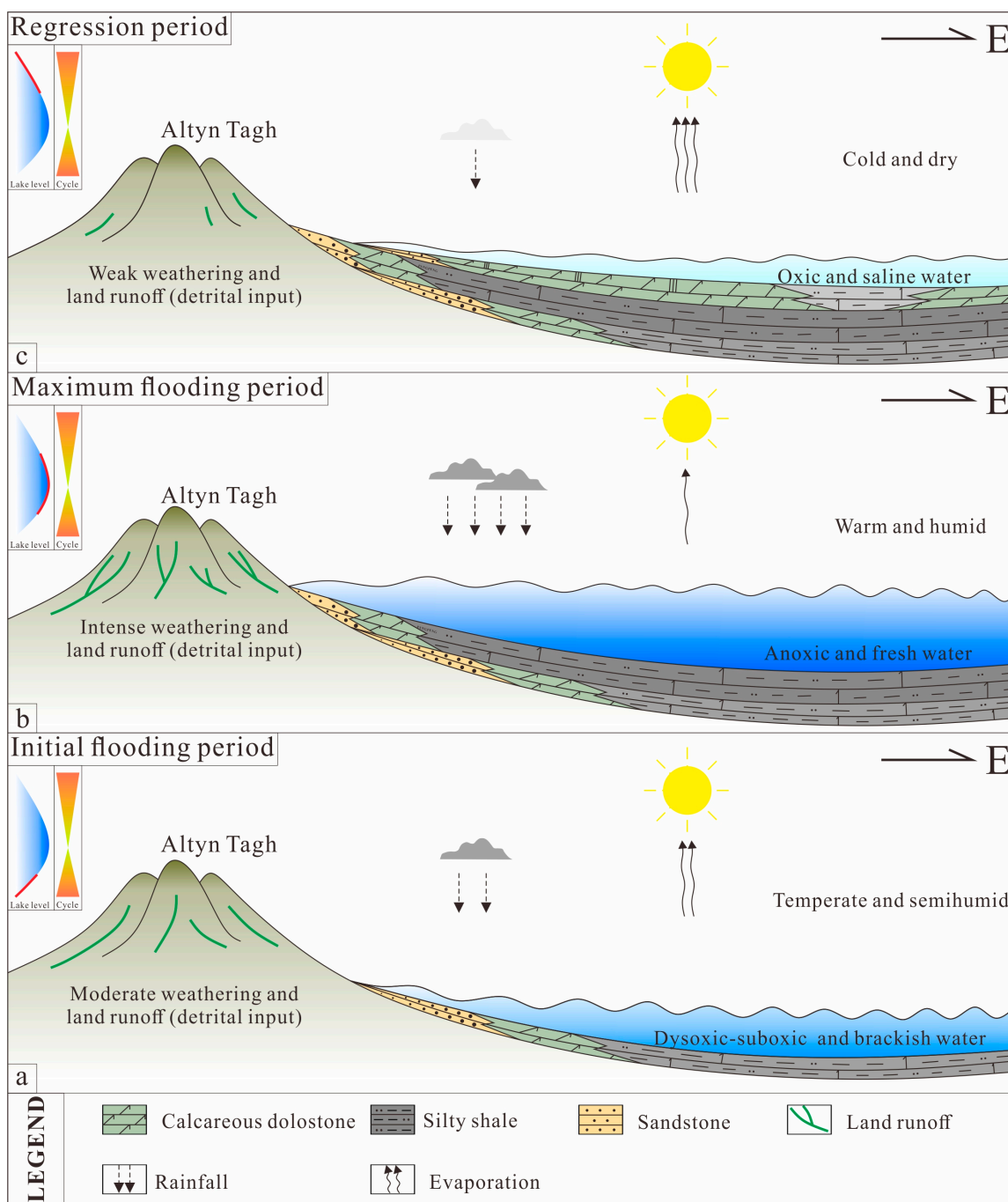


**Figure 11.** Synthesized paleoclimate–sedimentary model of lacustrine mixed rocks within high-frequency cycles of LGCG. (a) model of initial flooding period; (b) model of maximum flooding period; (c) model of regression period.

During the maximum flooding period, the lake basin was open, and the climate became warm and humid, characterized by intense weathering and land runoff (terrestrial input). With the change in paleoclimatic conditions, rainfall greatly exceeded evaporation, and the lake water level reached its peak within a high-frequency cycle, resulting in an anoxic and fresh paleowater environment. An abundance of terrigenous debris and nutrients was brought into the basin by intense chemical weathering and land runoff. Dark gray laminated silty shales were predominantly developed at the bottom of the lake (Figure 11b).

During the lake regression period, the lake basin was in a closed state, and the paleoclimate was cold and arid, accompanied by weak chemical weathering and detrital input

from land runoff. With the transformation of the paleoclimate, the evaporation surpassed the rainfall, resulting in a continuous decline in the lake level and an oxic paleowater environment. At the bottom of the lake, gray bedded gypsum-bearing calcareous dolostones were predominantly deposited (Figure 11c).

## 6. Conclusions

Variations in the paleoenvironment and paleoclimate in high-frequency cycles of the plateau saline lake were explored through integrated analyses of the petrology, mineralogy, organic geochemistry, and elemental geochemistry of mixed rocks from the Eocene LGCG in the southwestern Qaidam Basin. The following conclusions were drawn:

- (1) The mixed rocks of the Eocene LGCG in the southwestern Qaidam Basin are characterized by high-frequency cyclic sedimentation. A complete single high-frequency cycle is composed of three lithofacies from bottom to top: massive sandstone, laminated silty shale, and bedded calcareous dolostone.
- (2) Regular and superimposed variations in the paleoenvironment and paleoclimate were revealed in the mixed depositional systems, which exhibit high coherence with high-frequency sedimentary cycles.
- (3) From the bottom to the top of the cycles, there was a change in the water properties, from desalination and reduction to salinization and oxidation, which was controlled by the decrease in the lake level caused by the paleoclimate's transformation from warm and humid to cold and arid.

**Supplementary Materials:** The following supporting information can be downloaded at <https://www.mdpi.com/article/10.3390/min14010079/s1>: Table S1: Mineral composition of samples; Table S2: C and O isotopes of the studied samples; Table S3: Measured major, trace, and rare-earth element concentrations of the samples.

**Author Contributions:** Conceptualization, X.T., X.L. and K.W.; data curation, H.X., M.Z. and J.W.; funding acquisition, X.T. and X.L.; methodology, P.P.; project administration, P.P.; resources, X.T., K.W. and S.X.; software, H.X., Y.L. and W.D.; supervision, X.T.; writing—original draft, P.P.; writing—review and editing, S.W. and Y.X. All authors have read and agreed to the published version of the manuscript.

**Funding:** This research was co-funded by several funds and institutions, including China National Petroleum Corporation major science and technology project “Continental Shale Oil Large-scale Reserves Increasing and Exploration and Development Techniques” (Grant No.: 2023ZZ15), National Key Laboratory for Multi-resources Collaborative Green Production of Continental Shale Oil, Qinghai Provincial Middle and Young Talent Support Project of “Kunlun Talents · Science and Technology Leading Talents” Program (Grant No.: 2021QHJKXRCTJ06), and the Research and Innovation Fund for Graduate Students of Southwest Petroleum University (Grant No.: 2022KYCX037).

**Data Availability Statement:** The data presented in this study are available on request from the corresponding author.

**Acknowledgments:** We thank the academic editor and anonymous reviewers for their constructive suggestions, pertinent comments, and careful corrections, which greatly improved the quality of this manuscript.

**Conflicts of Interest:** Kunyu Wu, Songtao Wu, Shituan Xue, Haoting Xing, Yafeng Li, Menglin Zhang, and Juan Wang are employees of CNPC. The paper reflects the views of the scientists and not the company.

## References

1. Milankovitch, M. Canon of Insolation and the Ice Age Problem. *Math. Natl. Sci.* **1941**, *33*, 633. (In German)
2. Hays, J.D.; Imbrie, J.; Shackleton, N.J. Variations in the Earth's Orbit: Pacemaker of the Ice Ages. *Science* **1976**, *194*, 1121–1132. [[CrossRef](#)] [[PubMed](#)]
3. Tian, J.; Wu, H.; Huang, C.; Li, M.; Ma Chao Wang, P. Revisiting the Milankovitch Theory from the Perspective of the 405 ka Long Eccentricity Cycle. *Earth Sci.* **2022**, *47*, 3543–3568.

4. Imbrie, J. Astronomical Theory of the Pleistocene Ice Ages: A Brief Historical Review. *Icarus* **1982**, *50*, 408–422. [[CrossRef](#)]
5. Wu, H.C.; Zhang, S.H.; Feng, Q.L.; Fang, N.Q.; Yang, T.S.; Li, H.Y. Theoretical basin, research advancement and prospects of cyclostratigraphy. *Earth Sci.* **2011**, *36*, 409–428.
6. Zhang, Y.B.; Wang, G.H.; Yu, Z.W.; Zhao, Z.J.; Wang, M.J.; Sun, Y.P. Milankovitch cycles and high-frequency sequences of the Middle Permian Maokou Formation in Sichuan Basin. *J. Palaeogeogr.* **2013**, *15*, 777–787.
7. Zhong, S.K.; Tan, X.C.; Nie, W.C.; Zhang, D.F.; Yang, M.Y.; Lu, Z.X.; Zhang, X.Y.; Xiao, D. High-frequency cyclic sequence of the Ma56 submember of Middle Ordovician Majiagou Formation in Ordos Basin: Indication for sea-level change and sedimentary differentiation effect of Hengshan uplift. *J. Palaeogeogr.* **2020**, *24*, 245–260.
8. Coffey, B.P.; Read, J.F. Mixed carbonate-siliciclastic sequence stratigraphy of a Paleogene transition zone continental shelf, southeastern USA. *Sediment. Geol.* **2004**, *166*, 21–57. [[CrossRef](#)]
9. Parcell, W.C.; Williams, M.K. Mixed sediment deposition in a retro-arc foreland basin: Lower Ellis Group (M. Jurassic), Wyoming and Montana, USA. *Sediment. Geol.* **2005**, *177*, 175–194. [[CrossRef](#)]
10. García-Hidalgo, J.F.; Gil, J.; Segura, M.; Dominguez, C. Internal anatomy of a mixed siliciclastic-carbonate platform: The Late Cenomanian-Mid Turonian at the southern margin of the Spanish Central System. *Sedimentology* **2007**, *54*, 1245–1271. [[CrossRef](#)]
11. Palermo, D.; Aigner, T.; Geluk, M.; Poepplereiter, M.; Pipping, K. Reservoir potential of a lacustrine mixed carbonate/siliciclastic gas reservoir: The Lower Triassic Rogenstein in the Netherlands. *J. Petrol. Geol.* **2008**, *31*, 61. [[CrossRef](#)]
12. Xiong, Y.; Tan, X.; Wu, K.; Xu, Q.; Liu, Y.; Qiao, Y. Petrogenesis of the Eocene lacustrine evaporites in the western Qaidam Basin: Implications for regional tectonic and climate changes. *Sediment. Geol.* **2021**, *416*, 105867. [[CrossRef](#)]
13. Lehrmann, D.J.; Jiayong, W.; Enos, P. Controls on facies architecture of a large Triassic carbonate platform; the Great Bank of Guizhou, Nanpanjiang Basin, South China. *J. Sediment. Res.* **1998**, *68*, 311–326. [[CrossRef](#)]
14. Wright, E.E.; Hine, A.C.; Goodbred, S.L.; Locker, S.D. The effect of sea-level and climate change on the development of a mixed siliciclastic-carbonate, deltaic coastline: Suwannee River, Florida, USA. *J. Sediment. Res.* **2005**, *75*, 621–635. [[CrossRef](#)]
15. Xu, W.; Du, X.; Huang, X.; Song, Z.; Li, Z. Research Advances and Critical Issues of “mixed siliciclastic and carbonate sediments”. *Acta Sedimentol. Sin.* **2019**, *37*, 225–238.
16. Davis, R.A., Jr.; Cuffe, C.K.; Kowalski, K.A.; Shock, E.J. Stratigraphic models for microtidal tidal deltas; examples from the Florida Gulf coast. *Mar. Geol.* **2003**, *200*, 49–60. [[CrossRef](#)]
17. Li, G.; Wu, K.; Zhu, R.; Zhang, Y.; Wu, S.; Chen, Y.; Shen, Y.; Zhang, J.; Xing, H.; Li, Y.; et al. Enrichment model and high-efficiency production of thick plateau mountainous shale oil reservoir: A case study of the Yingxiongling shale oil reservoir in Qaidam Basin. *Acta Pet. Sin.* **2023**, *44*, 144–157.
18. Magalhães, A.J.C.; Gabaglia, G.R.; Fragoso, D.G.C.; Freire, E.B.; Lykawka, R.; Arregui, C.D.; Bruhn, C.H.L. High-resolution sequence stratigraphy applied to reservoir zonation and characterisation, and its impact on production performance-shallow marine, fluvial downstream, and lacustrine carbonate settings. *Earth Sci. Rev.* **2020**, *210*, 103325. [[CrossRef](#)]
19. Melo, A.H.; Magalhães, A.J.C.; Menegazzo, M.C.; Fragoso, D.G.C.; Florencio, C.P.; Lima-Filho, F.P. High-resolution sequence stratigraphy applied for the improvement of hydrocarbon production and reserves: A case study in Cretaceous fluvial deposits of the Potiguar basin, northeast Brazil. *Mar. Petrol. Geol.* **2021**, *130*, 105124. [[CrossRef](#)]
20. Feng, J.; Cao, J.; Hu, K.; Peng, X.; Chen, Y.; Wang, Y.; Wang, M. Dissolution and its impacts on reservoir formation in moderately to deeply buried strata of mixed siliciclastic-carbonate sediments, northwestern Qaidam Basin, northwest China. *Mar. Pet. Geol.* **2013**, *39*, 124–137. [[CrossRef](#)]
21. Zhang, W.; Jian, X.; Fu, L.; Feng, F.; Guan, P. Reservoir characterization and hydrocarbon accumulation in late Cenozoic lacustrine mixed carbonate-siliciclastic fine-grained deposits of the northwestern Qaidam basin, NW China. *Mar. Petrol. Geol.* **2018**, *98*, 675–686. [[CrossRef](#)]
22. Liu, Z.; Zhang, Y.; Song, G.; Li, S.; Long, G.; Zhao, J.; Wang, Y.; Gong, Q.; Xia, Z. Mixed carbonate rocks lithofacies features and reservoirs controlling mechanisms in a saline lacustrine basin in Yingxi area, Qaidam Basin, NW China. *Petrol. Explor. Dev.* **2021**, *48*, 80–94. [[CrossRef](#)]
23. Wu, H.; Liu, H.; Wang, L.; Gui, L.; Yang, C.; Wang, L. Mixed carbonate-siliciclastic reservoir characterization and hydrocarbon accumulation process of the Ganachaigou area in the western Qaidam Basin, Tibet Plateau. *Carbonates Evaporites* **2022**, *37*, 26. [[CrossRef](#)]
24. Xu, B.; Li, J.; Wu, Z.; Zhang, Y.; Cui, J. Sedimentary cycles of evaporites and their application in sequence division in the upper member of the Xiaganchaigou Formation in Yingxi Area, Southwestern Qaidam Basin, China. *Carbonates Evaporites* **2020**, *35*, 1–15. [[CrossRef](#)]
25. Yang, Y.; Sun, G.; Wang, Y.; Wu, J.; Jiang, Y.; Wang, M.; Li, J. Diagenesis and sedimentary environment of the lower Xiaganchaigou formation deposited during the Eocene/Oligocene transition in the Lenghu tectonic belt, Qaidam Basin, China. *Environ. Earth Sci.* **2020**, *79*, 1–14. [[CrossRef](#)]
26. Zhang, S.; Shao, M.; Wang, T.; Pei, Y.; Chen, B. Geochemistry of lacustrine carbonate rocks in southwestern Qaidam: Implications of silicate weathering and carbon burial triggered by the uplift of the Tibetan Plateau. *Int. J. Coal Geol.* **2023**, *265*, 104167. [[CrossRef](#)]
27. Xiong, Y.; Wu, K.Y.; Tan, X.C.; Zhang, Y.S.; Bo, Y.; Ling, R.; Wang, X.F. Influence of lake-level fluctuation on the mixed saline lacustrine carbonate reservoir: A case study. *J. Paleogeogr.* **2018**, *20*, 855–868.

28. Cheng, F.; Jolivet, M.; Fu, S.; Zhang, Q.; Guan, S.; Yu, X.; Guo, Z. Northward growth of the Qimen Tagh Range: A new model accounting for the Late Neogene strike-slip deformation of the SW Qaidam Basin. *Tectonophysics* **2014**, *632*, 32–47. [[CrossRef](#)]
29. Fu, S.T.; Ma, D.D.; Guo, Z.J.; Cheng, F. Strike-slip superimposed Qaidam Basin and its control on oil and gas accumulation, NW China. *Petrol. Explor. Dev.* **2015**, *42*, 712–722. [[CrossRef](#)]
30. Jia, C.Z.; Song, Y.; Wei, G.Q.; Zhao, M.J.; Liu, S.B.; Li, B.L. Geological features and petroleum accumulation in the foreland basins in central and western China. *Earth Sci. Front.* **2005**, *12*, 3–13.
31. Huang, C.; Yuan, J.; Cao, Z.; Zhang, S.M.; Wang, Y.; She, M. Simulate experiment study about the saline fluid-rock interaction in the clastic reservoir of the saline lacustrine basin. *Bull. Mineral. Petrol. Geochem.* **2015**, *34*, 343–348.
32. Liu, Z.G.; Zhu, C.; Li, S.M.; Xue, J.Q.; Gong, Q.S.; Wang, Y.Q.; Wang, P.; Xia, Z.Y.; Song, G.Y. Geological features and exploration fields of tight oil in the Cenozoic of western Qaidam Basin, NW China. *Petrol. Explor. Dev.* **2017**, *44*, 196–204. [[CrossRef](#)]
33. Qiao, Y.P.; Tan, X.C.; Liu, Y.; Xiong, Y.; Wu, K.Y.; Zhang, Y.S.; Yang, B.; Ren, L. Characteristics of High-frequency Lake-level Fluctuations in the Saline Lacustrine Basin and Its Geological Significance: A case study from the upper member of the Paleogene Lower Ganchaigou Formation in the Yingxi area, Qaidam Basin. *Acta Sedimentol. Sin.* **2020**, *38*, 1152–1165.
34. Chen, D.Q.; Shen, X.S.; Cui, J.; Lu, Y.P.; Huang, Y. Reservoir characteristics and controlling factors of deep diamictite in Yingxi area, Qaidam Basin. *Lithol. Reserv.* **2015**, *27*, 211–217.
35. Yi, D.; Wang, J.; Shi, Y.; Sun, X.; Ma, X.; Wang, P.; Li, Y. Evolution characteristic of gypsum-salt rocks of the upper member of Oligocene Lower Ganchaigou Fm in the Shizigou area, western Qaidam Basin. *Nat. Gas Ind.* **2017**, *4*, 390–398. [[CrossRef](#)]
36. Taylor, S.R.; McLennan, S.M. The Continental Crust: Its Composition and Evolution Geoscience Texts. *Blackwell Sci. Publ.* **1985**, *1*, 1–312.
37. Rieser, A.B.; Neubauer, F.; Liu, Y.J.; Ge, X.H. Sandstone provenance of north-western sectors of the intracontinental Cenozoic Qaidam basin, western China: Tectonic vs. climatic control. *Sediment. Geol.* **2005**, *177*, 1–18. [[CrossRef](#)]
38. Ye, C.C.; Yang, Y.B.; Fang, X.M.; Zhang, W.L. Late Eocene clay boron-derived paleosalinity in the Qaidam Basin and its implications for regional tectonics and climate. *Sediment. Geol.* **2016**, *346*, 49–59. [[CrossRef](#)]
39. Schreiber, B.C.; Tabakh, M.E. Deposition and early alteration of evaporites. *Sedimentology* **2000**, *47*, 215–238. [[CrossRef](#)]
40. Talbot, M.R. A review of the palaeohydrological interpretation of carbon and oxygen isotopic ratios in primary lacustrine carbonates. *Chem. Geol. Isot. Geosci.* **1990**, *80*, 261–279. [[CrossRef](#)]
41. Cai, G.Q.; Guo, F.; Liu, X.T.; Sui, S.L. Carbon and Oxygen Isotope Characteristics and Palaeoenvironmental Implications of Lacustrine Carbonate Rocks from the Shahejie Formation in the Dongying Sag. *Earth Environ.* **2009**, *37*, 347–354.
42. Yuan, J.; Huang, C.; Zhao, F.; Pan, X. Carbon and oxygen isotopic compositions, and palaeoenvironmental significance of saline lacustrine dolomite from the Qaidam Basin, Western China. *J. Petrol. Sci. Eng.* **2015**, *135*, 596–607. [[CrossRef](#)]
43. Yuan, J.Y.; Huang, C.G.; Cao, Z.L.; Li, Z.Y.; Wan, C.Z.; Xu, L.; Pan, X.; Wu, L.R. Carbon and oxygen isotopic composition of saline lacustrine dolomite and its palaeoenvironmental significance: A case study of Lower Eocene Ganchaigou Formation in western Qaidam Basin. *Geochimica* **2015**, *44*, 254–266.
44. Liu, C.L.; Zhao, Q.H.; Wang, P.X. Correlation between carbon and oxygen isotopic ratios of lacustrine carbonates and types of oil-producing paleolakes. *Geochimica* **2001**, *30*, 363–367.
45. Algeo, T.J.; Maynard, J.B. Trace-element behavior and redox facies in core shales of Upper Pennsylvanian Kansas-type cyclothems. *Chem. Geol.* **2004**, *206*, 289–318. [[CrossRef](#)]
46. Tribouvillard, N.; Algeo, T.J.; Lyons, T.; Riboulleau, A. Trace metals as paleoredox and paleoproductivity proxies: An update. *Chem. Geol.* **2006**, *232*, 12–32. [[CrossRef](#)]
47. Peng, J.W.; Fu, Q.L.; Larson, T.E.; Janson, X. Trace-elemental and petrographic constraints on the severity of hydrographic restriction in the silled Midland Basin during the late Paleozoic ice age. *Geol. Soc. Am. Bull.* **2021**, *133*, 57–73. [[CrossRef](#)]
48. Kimura, H.; Watanabe, Y. Oceanic anoxic at the Precambrian–Cambrian boundary. *Geology* **2001**, *29*, 995–998. [[CrossRef](#)]
49. McManus, J.; Berelson, W.M.; Klinkhammer, G.P.; Hammond, D.E.; Holm, C. Authigenic uranium: Relationship to oxygen penetration depth and organic carbon rain. *Geochim. Cosmochim. Acta* **2005**, *69*, 95–108. [[CrossRef](#)]
50. Brüske, A.; Weyer, S.; Zhao, M.Y.; Planavsky, N.J.; Wegwerth, A.; Neubert, N.; Dellwig, O.; Lau, K.V.; Lyons, T.W. Correlated molybdenum and uranium isotope signatures in modern anoxic sediments: Implications for their use as paleo-redox proxy. *Geochim. Cosmochim. Acta* **2020**, *270*, 449–474. [[CrossRef](#)]
51. Rimmer, S.M. Geochemical paleoredox indicators in Devonian–Mississippian black shales, central Appalachian Basin (USA). *Chem. Geol.* **2004**, *206*, 373–391. [[CrossRef](#)]
52. Costa, K.M.; Anderson, R.F.; McManus, J.F.; Winckler, G.; Middleton, J.L.; Langmuir, C.H. Trace element (Mn, Zn, Ni, V) and authigenic uranium (aU) geochemistry reveal sedimentary redox history on the Juan de Fuca Ridge, North Pacific Ocean. *Geochim. Cosmochim. Acta* **2018**, *236*, 79–98. [[CrossRef](#)]
53. Chappaz, A.; Gobeil, C.; Tessier, A. Controls on uranium distribution in lake sediments. *Geochim. Cosmochim. Acta* **2010**, *74*, 203–214. [[CrossRef](#)]
54. Yang, Y.B.; Fang, X.M.; Appel, E.; Galy, A.; Li, M.H.; Zhang, W.L. Late Pliocene–Quaternary evolution of redox conditions in the western Qaidam paleolake (NE Tibetan Plateau) deduced from Mn geochemistry in the drilling core SG-1. *Quat. Res.* **2013**, *80*, 586–595. [[CrossRef](#)]
55. Elzinga, E.J.; Tait, C.D.; Reeder, R.J.; Rector, K.D.; Donohoe, R.J.; Morris, D.E. Spectroscopic investigation of U (VI) sorption at the calcite-water interface. *Geochim. Cosmochim. Acta* **2004**, *68*, 2437–2448. [[CrossRef](#)]

56. Wright, J.; Schrader, H.; Holser, W.T. Paleoredox variations in ancient oceans recorded by rare earth elements in fossil apatite. *Geochim. Cosmochim. Acta* **1987**, *51*, 631–644. [[CrossRef](#)]
57. Wilde, P.; Quinby-Hunt, M.S.; Erdtmann, B.D. The whole-rock cerium anomaly: A potential indicator of eustatic sea-level changes in shales of the anoxic facies. *Sediment. Geol.* **1996**, *101*, 43–53. [[CrossRef](#)]
58. Tribovillard, N. Deep-water anoxia during the frasnian-famennian boundary events (la serre, france): An echo of a tectonically-induced late devonian oceanic anoxic event? *Terra Nova* **2004**, *16*, 288–295. [[CrossRef](#)]
59. Zhang, K.; Liu, R.; Liu, Z.; Li, L. Geochemical characteristics and geological significance of humid climate events in the Middle-Late Triassic (Ladinian-Carnian) of the Ordos Basin, central China. *Mar. Petrol. Geol.* **2021**, *131*, 105179. [[CrossRef](#)]
60. Xu, J.; Liu, Z.; Bechtel, A.; Meng, Q.; Sun, P.; Jia, J.; Cheng, L.; Song, Y. Basin evolution and oil shale deposition during Upper Cretaceous in the Songliao Basin (NE China): Implications from sequence stratigraphy and geochemistry. *Int. J. Coal Geol.* **2015**, *149*, 9–23. [[CrossRef](#)]
61. Xu, S.; Liu, Z.; Zhang, P.; Boak, J.M.; Liu, R.; Meng, Q. Characterization of depositional conditions for lacustrine oil shales in the Eocene Jijuntun formation, Fushun basin, NE China. *Int. J. Coal Geol.* **2016**, *167*, 10–30. [[CrossRef](#)]
62. Xiong, X.H.; Xiao, J.F. Geochemical indicators of sedimentary environments—A summary. *Earth Environ.* **2011**, *39*, 405–414.
63. Zhang, X.; Li, S.; Wang, X.; Zhao, X.; Yin, T. Expression of the early Aptian oceanic anoxic event (OAE) 1a in lacustrine depositional systems of East China. *Glob. Planet. Chang.* **2021**, *196*, 103370. [[CrossRef](#)]
64. Sheldon, N.D. Abrupt chemical weathering increase across the Permian–Triassic boundary. *Palaeogeogr. Palaeoclimatol. Palaeoecol.* **2006**, *231*, 315–321. [[CrossRef](#)]
65. Hermann, E.; Hochuli, P.A.; Bucher, H.; Brühwiler, T.; Hautmann, M.; Ware, D.; Roohi, G. Terrestrial ecosystems on North Gondwana in the aftermath of the end Permian mass extinction. *Gondwana Res.* **2011**, *20*, 630–637. [[CrossRef](#)]
66. Nesbitt, H.W.; Young, G.M. Early Proterozoic climates and plate motions inferred from major element chemistry of lutites. *Nature* **1982**, *299*, 715–717. [[CrossRef](#)]
67. Fedo, C.M.; Nesbitt, H.W.; Young, G.M. Unraveling the effects of potassium metasomatism in sedimentary rocks and paleosols, with implications for paleoweathering conditions and provenance. *Geology* **1995**, *23*, 921–924. [[CrossRef](#)]
68. Yang, J.; Cawood, P.A.; Du, Y.; Feng, B.; Yan, J. Global continental weathering trends across the Early Permian glacial to postglacial transition: Correlating highland low-paleolatitude sedimentary records. *Geology* **2014**, *42*, 835–838. [[CrossRef](#)]
69. Yan, D.; Chen, D.; Wang, Q.; Wang, J. Large-scale climatic fluctuations in the latest Ordovician on the Yangtze block, South China. *Geology* **2010**, *38*, 599–602. [[CrossRef](#)]
70. Shen, J.; Algeo, T.J.; Hu, Q.; Xu, G.Z.; Zhou, L.; Feng, Q.L. Volcanism in South China during the Late Permian and its relationship to marine ecosystem and environmental changes. *Glob. Planet. Chang.* **2013**, *105*, 121–134. [[CrossRef](#)]
71. Xu, G.; Feng, Q.; Deconinck, J.; Shen, J.; Zhao, T.; Young, A.L. High-resolution clay mineral and major elemental characterization of a Permian–Triassic terrestrial succession in southwestern China: Diagenetic and paleoclimatic/paleoenvironmental significance. *Palaeogeogr. Palaeoclimatol. Palaeoecol.* **2017**, *481*, 77–93. [[CrossRef](#)]
72. McLennan, S.M. Weathering and global denudation. *J. Geo.* **1993**, *101*, 295–303. [[CrossRef](#)]
73. Cox, R.; Lowe, D.R.; Cullers, R.L. The influence of sediment recycling and basement composition on evolution of mudrock chemistry in the southwestern United States. *Geochem. Cosmochim. Acta* **1995**, *59*, 2919–2940. [[CrossRef](#)]
74. Zhang, K.; Liu, R.; Liu, Z. Sedimentary sequence evolution and organic matter accumulation characteristics of the Chang 8–Chang 7 members in the Upper Triassic Yanchang Formation, southwest Ordos Basin, central China. *J. Petrol. Sci. Eng.* **2021**, *196*, 107751. [[CrossRef](#)]
75. Panahi, A.; Young, G.M.; Rainbird, R.H. Behavior of major and trace elements (including REE) during Paleoproterozoic pedogenesis and diagenetic alteration of an Archean granite near Ville Marie, Qu ´ebec, Canada. *Geochem. Cosmochim. Acta* **2000**, *64*, 2199–2220. [[CrossRef](#)]
76. Gulbranson, E.L.; Montanez, I.P.; Tabor, N.J.; Oscar Limarino, C. Late Pennsylvanian aridification on the southwestern margin of Gondwana (Paganzo Basin, NW Argentina): A regional expression of a global climate perturbation. *Palaeogeogr. Palaeoclimatol. Palaeoecol.* **2015**, *417*, 220–235. [[CrossRef](#)]
77. Cao, H.; Kaufman, A.J.; Shan, X. Coupled isotopic evidence for elevated pCO<sub>2</sub> and nitrogen limitation across the Santonian–Campanian transition. *Chem. Geol.* **2019**, *504*, 136–150. [[CrossRef](#)]
78. Cao, Y.; Song, H.; Algeo, T.J.; Chu, D.; Du, Y.; Tian, L.; Wang, Y.; Tong, J. Intensified chemical weathering during the Permian–Triassic transition recorded in terrestrial and marine successions. *Palaeogeogr. Palaeoclimatol. Palaeoecol.* **2019**, *519*, 166–177. [[CrossRef](#)]
79. Zhang, Y.; Tang, P.; Jin, J.; Sun, S.; Wang, Y. Climate change in the subtropical Paleo-Tethys before the late Ordovician glaciation. *Glob. Planet. Chang.* **2021**, *199*, 103432. [[CrossRef](#)]
80. Liu, B.; Song, Y.; Zhu, K.; Su, P.; Ye, X.; Zhao, W. Mineralogy and element geochemistry of salinized lacustrine organic-rich shale in the Middle Permian Santanghu Basin: Implications for paleoenvironment, provenance, tectonic setting and shale oil potential. *Mar. Petrol. Geol.* **2020**, *120*, 104569. [[CrossRef](#)]
81. Sharps, R.; Li, Y.; McWilliams, M.; Li, Y. Paleomagnetic investigation of upper Permian sediments in the south Junggar Basin, China. *J. Geophys. Res. Solid Earth.* **1992**, *97*, 1753–1765. [[CrossRef](#)]

82. Li, G.; Zhu, R.; Zhang, Y.; Chen, Y.; Cui, J.; Jiang, Y.; Wu, K.; Shen, J.; Xian, C.; Liu, H. Geological characteristics, evaluation criteria and discovery significance of Paleogene Yingxiongling shale oil in Qaidam Basin, NW China. *Petrol. Explor. Dev.* **2022**, *49*, 18–31. [[CrossRef](#)]
83. Jiang, Q.; Ma, Y.; Shen, Y.; Guo, R.; Gao, X.; Liu, B.; Wu, K. High-frequency redox variations of the Eocene cyclic lacustrine sediments in the Yingxi area, western Qaidam Basin, China. *J. Asian Earth Sci.* **2019**, *174*, 135–151. [[CrossRef](#)]

**Disclaimer/Publisher’s Note:** The statements, opinions and data contained in all publications are solely those of the individual author(s) and contributor(s) and not of MDPI and/or the editor(s). MDPI and/or the editor(s) disclaim responsibility for any injury to people or property resulting from any ideas, methods, instructions or products referred to in the content.